Effect of Magnetic Forces and Magnetostriction on the Stator Vibrations of a Bearingless Synchronous Reluctance Motor

Victor Mukherjee[1,4], Paavo Rasilo[2], Floran Martin[1] and Anouar Belahcen[1,3] (*Senior member, IEEE*)

[1] Aalto University, Department of Electrical Engineering and Automation, Espoo 02150, Finland
[2] Tampere University, Faculty of Information Technology and Communication Sciences, Tampere 33014, Finland
[3] Tallinn University of Technology, Department of Electrical Power Engineering and Mechatronics, Tallinn 19086, Estonia.
[4] VTT Technical Research Centre of Finland, Espoo 02044, Finland

The stator vibrations of a bearingless synchronous reluctance motor are investigated with simulations. The influence of the Maxwell stress tensor and magnetostriction on the stator vibrations is studied at different operational conditions. An energy-based magnetomechanical model of iron core is implemented and the influence of the magnetostriction in the iron core on the stator vibrations are further investigated and compared with the case where the magnetostriction is not modeled. The objective of the research is to find out how the stator vibrations can be used to detect the off-center rotor position. The results show that a single frequency component is not able to assess this phenomenon but a combination of two components makes it possible.

***Index Terms*— Bearingless Machine, Eccentricity, Magnetostriction, Maxwell Stress, Mechanical Vibrations, Synchronous Reluctance Motor.**

I. Introduction

A Bearingless Motor is an integration of the functionality of the active magnetic bearing principle in a conventional motor. For this purpose, an additional $p\pm1$ pole pair winding is assembled with a p pole pair main winding in the same slots to create an uneven distribution of the flux density in the airgap. The direction of the current space vector determines the direction of the electromagnetic force acting on the rotor. Upon controlling this electromagnetic force, an appropriate levitation of the rotor can be achieved [1], [2]. For the control purpose, the rotor position is sensed with eddy-current sensors [3], or without sensors through the use of an observer [4]. In both cases, the measured rotor position depends on the accuracy of the sensors or the observer. Hence, inaccurate estimation of the rotor position will result in a rotor eccentricity during the machine operation. Such a static eccentricity with a given amplitude in some direction of the air-gap is very common in bearingless machines. In addition, due to the lack of an ideal levitation control in the machine [5], the rotor center point does not always stay at the stator center point, which means that the rotor is always subjected to a certain amount of eccentricity. The rotor eccentricity further changes the magnetic flux density distribution in the air gap and thus the levitation force acting on the rotor. Meanwhile, the magnetic forces and the magnetostriction of the iron core produce vibrations of the stator, which can be monitored and used to assess the level of eccentricity in the machine.

Eccentricity in any regular machines is considered as a fault, and numerous studies have been performed to understand the eccentricity fault by computing and measuring the vibration of the machine. In general, most of the studies of the vibration consider a weak coupling between the electromagnetic model and the mechanical model. They also systematically ignore the effect of magnetostriction [6]. A multiaxial magnetomechanical material model has been lately developed and incorporated in the finite element (FE) analysis of an induction machine [7], [8]. The analysis showed a significant deformation of the stator cause by the magnetostriction together with the Maxwell stress tensor.

So far, the vibrations of the bearingless synchronous reluctance machines (BSynRM) have not been thoroughly studied. The aim of the work presented in this paper is to fill this gap. The three major contributions of this paper are the investigations on how the stator vibrations of a BSynRM are affected by (i) the effect of the Maxwell stress and the magnetostriction, (ii) the levitation forces, and (iii) the combined effect of the levitation and eccentricity forces. For these purposes, two different models of the magnetic material in the machine are implemented in the FE simulation. The aim of these investigations is to assess the possibility of using the vibrations as an indicator of the rotor off center position.

In the following, a short description of the models is given and their application to the machine under study is explained. The last part of the paper presents the results of the investigations and their discussions.

II. Model Description

In this work, two models of the magnetic material are used. The first one is the conventional nonlinear magnetic and linear elastic model coupled in a weak unidirectional way. It does not account for the magnetostriction of the material or the dependence of the material magnetic properties on its stress state. The second model is the energy based magnetomechanical model proposed in [7], [8], which is implemented here for the FE simulations of a BSynRM. This material model is based on a Helmholtz free energy density ψ

Manuscript received November 11, 2018; revised XX YY, 2018; accepted XX YY, 2018. Date of publication XX YY, 2019; date of current version XX YY, 2019. Corresponding author: V. Mukherjee (e-mail: victor.mukherjee@aalto.fi). Color versions of one or more of the figures in this paper are available online at http://ieeexplore.ieee.org.
Digital Object Identifier (inserted by IEEE).

which is expressed as a function of five scalar invariants. The invariants are further expressed as a function of the flux density $\boldsymbol{B}$ and the total strain tensor $\boldsymbol{\varepsilon}$ as

$$I_1 = \mathrm{tr}\,\boldsymbol{\varepsilon}, \quad I_2 = \mathrm{tr}\,\boldsymbol{\varepsilon}^2$$
$$I_4 = \frac{\boldsymbol{B}\cdot\boldsymbol{B}}{B_{\mathrm{ref}}^2}, \quad I_5 = \frac{\boldsymbol{B}\cdot\left(\tilde{\boldsymbol{\varepsilon}}\boldsymbol{B}\right)}{B_{\mathrm{ref}}^2}, \quad I_6 = \frac{\boldsymbol{B}\cdot\left(\tilde{\boldsymbol{\varepsilon}}^2\boldsymbol{B}\right)}{B_{\mathrm{ref}}^2} \quad . \tag{1}$$

where B_{ref} = 1 T is a reference value of the flux density, and tr refers to the trace. The deviatoric strain tensor is given as

$$\tilde{\boldsymbol{\varepsilon}} = \boldsymbol{\varepsilon} - \frac{1}{3}(\mathrm{tr}\,\boldsymbol{\varepsilon})\boldsymbol{I} \quad . \tag{2}$$

The magnetic field strength and the stress tensor are derived from the energy as

$$\boldsymbol{H}(\boldsymbol{B},\boldsymbol{\varepsilon}) = \left(\frac{\partial\psi(\boldsymbol{B},\boldsymbol{\varepsilon})}{\partial\boldsymbol{B}}\right)^{\mathrm{T}} \text{ and } \boldsymbol{\sigma}(\boldsymbol{B},\boldsymbol{\varepsilon}) = \frac{\partial\psi(\boldsymbol{B},\boldsymbol{\varepsilon})}{\partial\boldsymbol{\varepsilon}}. \tag{3}$$

An expression for ψ is provided in [7], where the model is fitted with measurements at various loading states.

The magneto-mechanical analysis of the BSynRM is carried out with the FE method formulated in terms of the magnetic vector potential $\boldsymbol{a}$ and the displacement vector $\boldsymbol{u}$ for the magnetostatic and the elastodynamic problems respectively. The energy based model is applied to the iron core, whereas the contribution of the Maxwell stress tensor is accounted for from both the air and the iron. In a 2D problem, the vector potential and the displacements are expressed in terms of the nodal shape functions, whereas the magnetic flux density and the strain are computed through the spatially differentiated shape functions as

$$\boldsymbol{B} = \boldsymbol{D}_{\mathrm{mag}}\boldsymbol{a} \quad \text{and} \quad \varepsilon = \boldsymbol{D}_{\mathrm{mech}}\boldsymbol{u}, \tag{4}$$

where

$$\boldsymbol{D}_{\mathrm{mag}}^{\mathrm{T}} = \begin{bmatrix} \frac{\partial \boldsymbol{N}}{\partial y} & -\frac{\partial \boldsymbol{N}}{\partial x} \end{bmatrix} \text{ and } \boldsymbol{D}_{\mathrm{mech}}^{\mathrm{T}} = \begin{bmatrix} \frac{\partial \boldsymbol{N}}{\partial x} & 0 & \frac{\partial \boldsymbol{N}}{\partial y} \\ 0 & \frac{\partial \boldsymbol{N}}{\partial y} & \frac{\partial \boldsymbol{N}}{\partial x} \end{bmatrix}, \tag{5}$$

The discrete coupled system for the iron core is expressed as

$$\left\langle \boldsymbol{D}_{\mathrm{mag}}^{\mathrm{T}} H(\boldsymbol{B},\boldsymbol{\varepsilon}) \right\rangle = 0$$
$$\left\langle \boldsymbol{D}_{\mathrm{mech}}^{\mathrm{T}}\left[\boldsymbol{\sigma}(\boldsymbol{B},\boldsymbol{\varepsilon}) - \boldsymbol{\sigma}_0\right]\right\rangle + \boldsymbol{C}\boldsymbol{v} + \boldsymbol{M}\frac{d\boldsymbol{v}}{dt} = -\left\langle \begin{bmatrix} \boldsymbol{N}^{\mathrm{T}} \\ \boldsymbol{N}^{\mathrm{T}} \end{bmatrix} f \right\rangle, \tag{6}$$
$$\frac{d\boldsymbol{u}}{dt} - \boldsymbol{v} = 0$$

In the above expression, $\boldsymbol{M}$ and $\boldsymbol{C}$ are the mass and damping matrices for the mechanical equations, $\boldsymbol{v}$ is the nodal velocity vector, $\boldsymbol{\sigma}_0$ is a pre-stress and $\boldsymbol{H}$ is the magnetic field strength. The brackets $\langle \cdot \rangle$ denote integration over the studied domain. Applying the backward Euler integration scheme and the Newton-Raphson iteration method, the Jacobian matrix is assembled as shown in (7).

The magnetic parts of the equations are also coupled with the circuit equations of the main and additional winding in both models, so that the windings can be supplied with voltage sources. In the simulations, the rotor is considered at a constant speed and a fixed lateral position and the airgap is re-meshed at every time step.

$$\begin{bmatrix} \left\langle \boldsymbol{D}_{\mathrm{mag}}^{\mathrm{T}} \frac{\partial \boldsymbol{H}}{\partial \boldsymbol{B}} \boldsymbol{D}_{\mathrm{mag}} \right\rangle & \left\langle \boldsymbol{D}_{\mathrm{mag}}^{\mathrm{T}} \frac{\partial \boldsymbol{H}}{\partial \boldsymbol{\varepsilon}} \boldsymbol{D}_{\mathrm{mech}} \right\rangle & 0 \\ \left\langle \boldsymbol{D}_{\mathrm{mech}}^{\mathrm{T}} \frac{\partial \boldsymbol{\sigma}}{\partial \boldsymbol{B}} \boldsymbol{D}_{\mathrm{mag}} \right\rangle & \left\langle \boldsymbol{D}_{\mathrm{mech}}^{\mathrm{T}} \frac{\partial \boldsymbol{\sigma}}{\partial \boldsymbol{\varepsilon}} \boldsymbol{D}_{\mathrm{mech}} \right\rangle & \boldsymbol{C} + \frac{1}{\Delta t} M \\ 0 & \frac{1}{\Delta t}\boldsymbol{I} & -\boldsymbol{I} \end{bmatrix} \tag{7}$$

III. Application to the Prototype Machine

The described models are applied to a prototyped BSynRM, the parameters of which are given in Table I. The mesh used in both models and the computed flux density distribution of the motor at the rated torque and levitation are presented in Fig. 1. In this case, the main winding and additional winding fluxes add to each other in the positive y axis and oppose each other in the negative y axis. As a result, the stator is more saturated in the upper part than in the lower one.

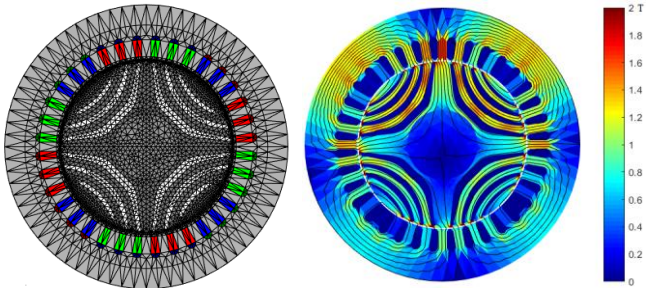

(a) (b)

Fig. 1. (a) FE mesh, where the additional winding can be seen at the bottom of the slots. (b) Computed flux density distribution in the motor at rated torque and levitation conditions.

TABLE I
PARAMETERS OF THE ANALYZED MACHINE

Parameter	Value
Rated power	4.8 kW
Rated voltage (main/additional)	360/40 V
Rated current (main/additional)	14.8/1 A
No-load current (main)	10.6 A
Connection	Star
Frequency (main and additional)	50 Hz
Pole pairs (main/additional)	2/1
Stator outer diameter	235 mm
Stator inner diameter	145 mm
Number of slots	36
Airgap	1 mm

The prototype machine is presented in Fig. 2. Active magnetic bearings (AMBs) are used on both sides of the shaft, so that the machine can be operated without any active control of the levitation.

IV. Results and Discussion

The prototype machine has been simulated with both models under the same conditions as it has been measured. The supply is a sinusoidal voltage from the grid, and the synchronization has been performed by an external motor, which was removed afterwards. The simulated and measured

current waveforms are presented in Fig. 3 for both the main and additional windings. In this case, the machine is operated without any control system and without any load.

Search coils with 5 turns have been placed around each of the Q stator teeth of the stator to enable the measurement of the flux through each tooth. The radial flux-density distribution $B_r(\theta)$ in the air gap is approximated by the average flux densities $B_{r,i}$, $i = 1, \ldots, Q$, through each tooth, obtained by dividing the tooth fluxes with the tooth surface areas. The total force is obtained as

$$\boldsymbol{F}_T = \frac{rl\pi}{\mu_0 Q}\sum_{i=1}^{Q} B_{r,i}^2 \boldsymbol{u}_i \,, \tag{8}$$

where $\boldsymbol{u}_i$ is the radial unit direction vector of tooth i.

In Fig. 4, the measured and modeled total electromagnetic forces are compared for different auxiliary winding currents. The measured current and electromagnetic forces show good agreement with the FE analysis, which proves the magnetic validity of the models.

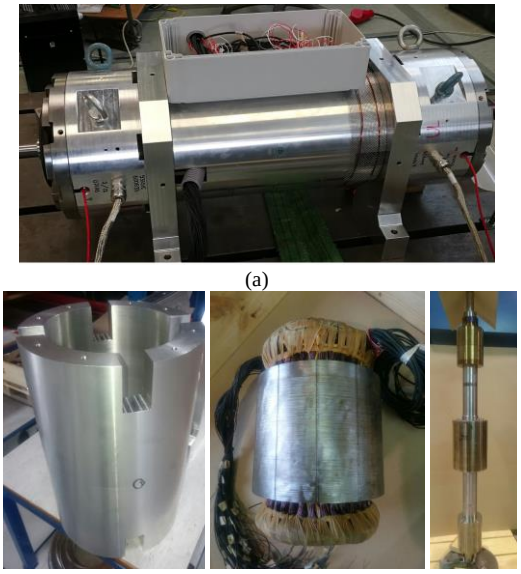

(a) (b) (c) (d)

Fig. 2. (a) Prototype setup, (b) Aluminum frame (c) stator, and (d) rotor

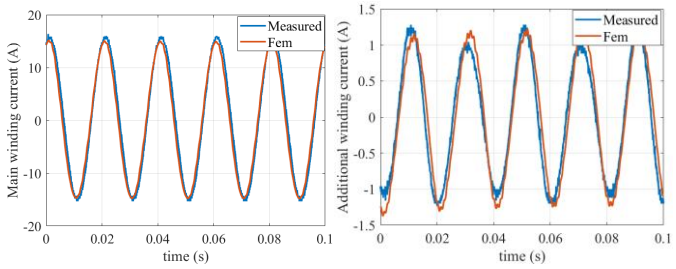

(a) (b)

Fig. 3. Current waveform of (a) main winding, and (b) additional winding.

Once the global operation parameters of the machine have been validated, the vibrational behavior is studied. When the rotor is displaced from the stator center point to any certain direction, the stator will vibrate differently than when the rotor is at the center point. To understand how the stator vibrations are influenced by the rotor eccentricity along with the additional winding excitation, we simulated the machine under different operation conditions and with both models. It is worth to remember that the eccentricity-related harmonics have also $p\pm1$ pole pair components, similar to the one generated by the additional winding. Furthermore, the contribution of the magnetostriction to these vibrations has not been clarified up to now. The computed stator deformation at a given time step and the displacement of a node on the outer stator boundary as a function of time are shown in Fig. 5. These results are for the rated operation where the rotor is at the center position. Considering the magnetostriction in the core changes the stator deformation by almost 8 % with respect to the linear elasticity case.

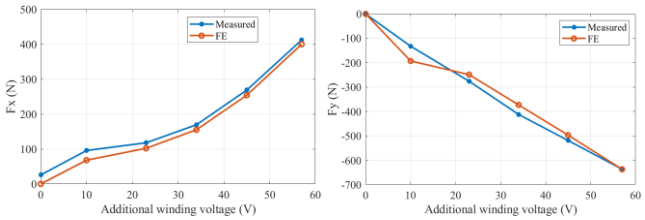

(a) (b)

Fig. 4. Comparison of the measured and simulated forces both as functions of the terminal additional winding voltage in (a) x axis, and (b) y axis

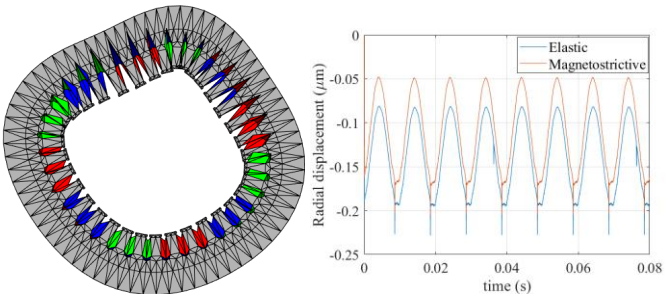

(a) (b)

Fig. 5. Simulated (a) deformation of the stator scaled by $5\text{x}10^4$, and (b) displacement of an outer stator boundary node.

The vibrations of the stator are further investigated for the three following operation conditions:

a) Only the main winding is supplied, no eccentricity.
b) Both windings are supplied, no eccentricity.
c) Both windings are supplied, and the rotor is eccentric in the positive x direction.

In each case, the simulations have been done, considering the stator and rotor cores as either linear elastic or magnetostrictive material. The results are presented in Fig. 6. From the above simulations it looks like the main interesting harmonics are 200 Hz and 400 Hz, which show changes in the radial acceleration under different operating conditions. The behavior of these frequency components is further investigated. The rotor is displaced from the center to the positive x-axis at different amplitudes, while the main and additional windings are supplied with the rated voltages. The computed radial accelerations are shown in Fig. 7 (a). As the magnetic flux density is highly non-uniform due the excitation of the additional winding, the direction of the eccentricity is also very important. To assess this issue, the radial accelerations of the 200 Hz and 400 Hz components are computed at different angles of the eccentricity with a fixed

amplitude of 30 %. The corresponding accelerations are shown in Fig. 7(b).

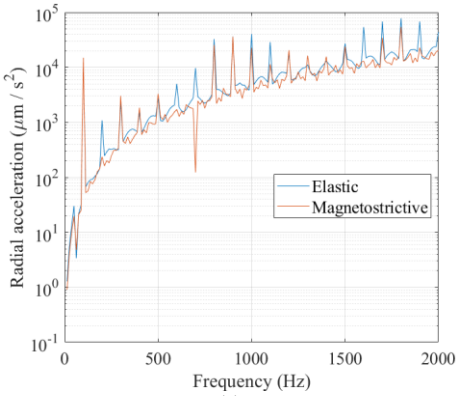

(a)

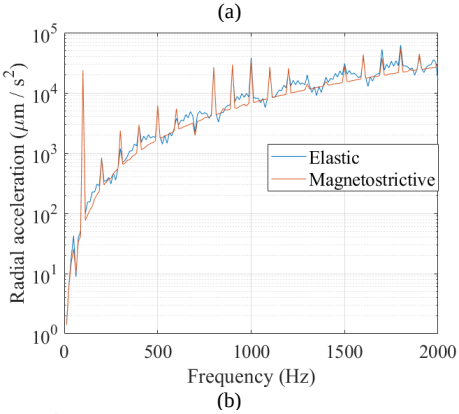

(b)

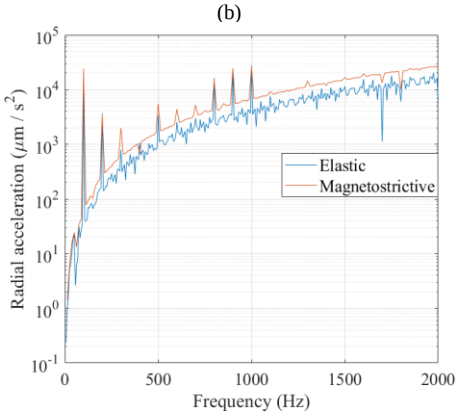

(c)

Fig. 6. Simulated radial acceleration of a stator outer node under the above mentioned operation conditions.

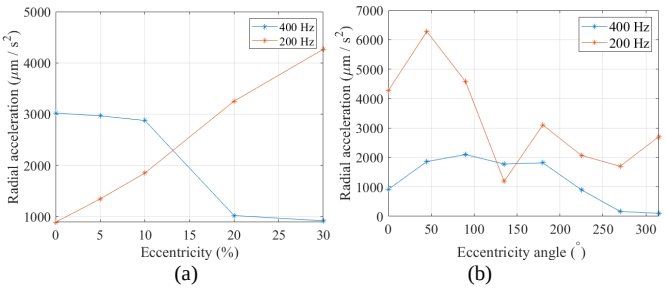

(a) (b)

Fig. 7. Radial accelerations of a stator outer node when the rotor is eccentric (a) with different amplitudes towards the positive x axis, and (b) with a fixed 0.03 mm amplitude at different direction.

The results of Fig. 7 show that a single harmonic of vibrations does not uniquely detect the rotor eccentricity as the amplitude of these vibrations depends strongly on the eccentricity direction. However, a combination of both 200 Hz and 400 Hz components can be used to assess the rotor eccentricity in the BSynRM, making it possible to tune either the position sensor or the observer in case of sensorless operation.

V. Conclusion

This paper shows that the eccentric position of the rotor of a BSynRM can be detected through two frequency components of the vibrations. For this purpose, we implemented two models of the magnetic material in the FE magnetomechanical simulation of a prototype BSynRM and computed the vibrations under different operating condition and with different material models. The simulations show that the magnetostriction in this machine with this number of stator poles can have either a reducing or amplifying effect on the vibrations depending on the combination of the levitation and the eccentricity. An experimental validation of the models from the point of view of global quantities such as currents and total force on the rotor is achieved too, however, a validation through vibration measurements is still lacking.

Acknowledgment

The authors acknowledge the Academy of Finland for financial support. This work was supported in part by the Estonian Research Council under the Grant number PUT1260. The authors thank Dr. Seppo Saarakkala and Dr Kari Tammi for their guidance in the prototype setup and measurement.

References

[1] A. Chiba, *Magnetic bearings and bearingless drives*, Amsterdam: Elsevier/Newnes, 2005.

[2] M. Takemoto, K. Yoshida, N. Itasaka, Y. Tanaka, A. Chiba and T. Fukao, "Synchronous Reluctance Type Bearingless Motors with Multi-flux Barriers," *2007 Power Conversion Conference - Nagoya*, Nagoya, 2007, pp. 1559-1564

[3] L. Chen and W. Hofmann, "Speed Regulation Technique of One Bearingless 8/6 Switched Reluctance Motor With Simpler Single Winding Structure," in *IEEE Transactions on Industrial Electronics*, vol. 59, no. 6, pp. 2592-2600, June 2012.

[4] K. Raggl, B. Warberger, T. Nussbaumer, S. Burger and J. W. Kolar, "Robust Angle-Sensorless Control of a PMSM Bearingless Pump," in *IEEE Transactions on Industrial Electronics*, vol. 56, no. 6, pp. 2076-2085, June 2009.

[5] S. E. Saarakkala, V. Mukherjee, M. Sokolov, M. Hinkkanen and A. Belahcen, "Analytical Model Including Rotor Eccentricity for Bearingless Synchronous Reluctance Motors," In Proc. ICEM, Alexandroupoli, Greece, 2018, pp. 1388-1394.

[6] A. Sinervo, A. Laiho and A. Arkkio, "Low-Frequency Oscillation in Rotor Vibration of a Two-Pole Induction Machine With Extra Four-Pole Stator Winding," in *IEEE Transactions on Magnetics*, vol. 47, no. 9, pp. 2292-2302, Sept. 2011.

[7] K. Fonteyn, A. Belahcen, R. Kouhia, P. Rasilo and A. Arkkio, "FEM for Directly Coupled Magneto-Mechanical Phenomena in Electrical Machines," in *IEEE Transactions on Magnetics*, vol. 46, no. 8, pp. 2923-2926, Aug. 2010.

[8] P. Rasilo *et al.*, "Multiaxial magneto-mechanical modelling of electrical machines with hysteresis," in Proc. PEMD, Glasgow, 2016, pp. 1-6.